Journal of Laser Applications

RESEARCH ARTICLE | SEPTEMBER 29 2023

Numerical and experimental investigation of the melt removal mechanism and burr formation during laser cutting of metals

Special Collection: Proceedings of the International Congress of Applications of Lasers & Electro-Optics (ICALEO 2023)

S. Stoyanov ; D. Petring ; F. Piedboeuf ; M. Lopes ; F. Schneider

J. Laser Appl. 35, 042028 (2023)
https://doi.org/10.2351/7.0001182

Journal of Laser Applications ARTICLE pubs.aip.org/lia/jla

Numerical and experimental investigation of the melt removal mechanism and burr formation during laser cutting of metals

Cite as: J. Laser Appl. **35**, 042028 (2023); doi: 10.2351/7.0001182
Submitted: 17 July 2023 · Accepted: 6 September 2023 ·
Published Online: 29 September 2023

S. Stoyanov,[1] D. Petring,[1] F. Piedboeuf,[2] M. Lopes,[2] and F. Schneider[1]

AFFILIATIONS

[1]Fraunhofer Institute for Laser Technology ILT, Steinbachstr. 15, Aachen 52074, Germany
[2]Chair for Laser Technology LLT, RWTH Aachen University, Steinbachstr. 15, Aachen 52074, Germany

Note: Paper published as part of the special topic on Proceedings of the International Congress of Applications of Lasers & Electro-Optics 2023.

ABSTRACT

During laser fusion cutting, burr forms when the molten metal does not sufficiently exit the interaction zone. When it forms on the lower edge of the cut flank, burr becomes a factor limiting quality. Previous research has shown that a temporally regular and spatially localized melt flow can prevent the formation of burr. However, the high dynamics of the subprocesses involved can cause intrinsic instabilities that disrupt the flow and reduce the efficiency of the melt ejection. This paper presents a study on the correlation between process parameters, melt flow properties, and burr formation. It includes an experimental observation of the melt-flow dynamics using high-speed videography. In addition, a Computational Fluid Dynamics model was set up to examine fundamental flow properties, some of which are not observable experimentally. The dependency of the burr formation on the liquid Weber and Reynolds numbers is analyzed, and it is demonstrated how the magnitude and allocation of vapor pressure gradients in the kerf decisively affect melt ejection and burr formation. Additionally, a previously unknown melt ejection regime is identified in the thick section range, which occurs at feed rates close to the maximum cutting speed under specific high-power process conditions. This regime is characterized by a significantly increased process efficiency that could open up a new high-speed process window.

Key words: laser fusion cutting, burr formation, supersonic gas flow, melt flow, multiphase simulation, CFD, high-speed imaging

I. INTRODUCTION

In laser fusion cutting, burr is formed when the molten material does not completely exit the cut kerf but adheres to the lower cut edge and resolidifies. The variety of possible burr topologies is large and depends on the amount of adhering melt and the dynamics of the melt flow (see Fig. 1). Yet, regardless of its shape, burr is undesirable from a technical point of view—because it limits or prevents the usability of the workpiece, and from an esthetic point of view—because it affects the appearance of the cut edge. Therefore, an additional deburring step is often carried out.

In laser fusion cutting of metals, laser radiation is focused on the material so that local melting takes place in the interaction zone. That melt is continuously expelled from the interaction zone by the cutting gas jet (typically nitrogen), which flows coaxially to the laser beam via a cutting nozzle.

The relative movement of the laser beam and the workpiece creates a cut channel or kerf. The melt flow within the kerf is confined by the free surfaces of absorption and the melting front, as depicted in Fig. 2. The absorption front is the surface of the melt illuminated by the laser beam. The melting front is the interface between the solid and liquid materials.

The melt is accelerated by the driving forces of the gas jet (pressure and shear force) and, if present, by vapor pressure gradients. It is decelerated by internal friction (viscosity) and capillary forces.[1] The interaction of these forces creates complex melt flow

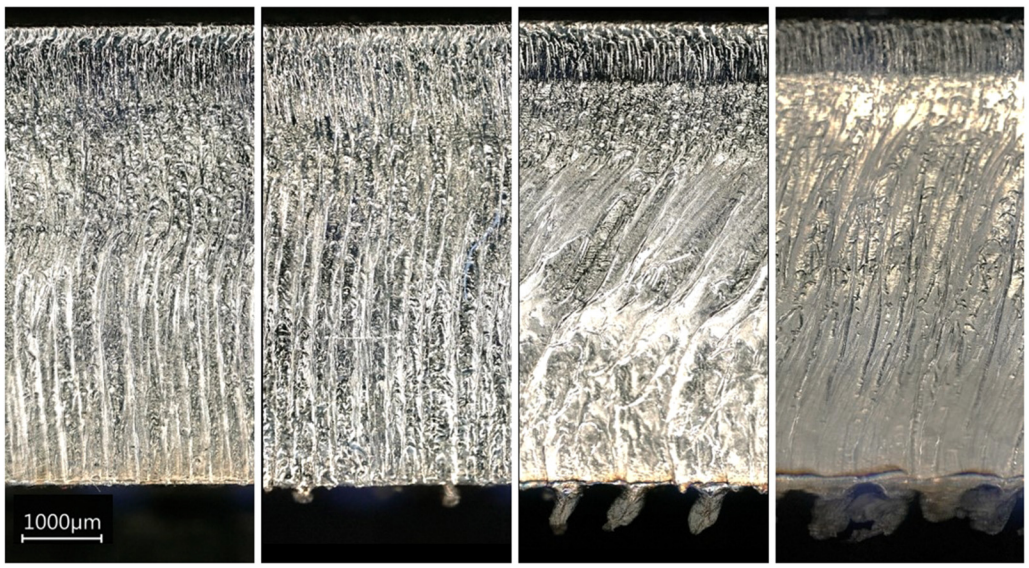

FIG. 1. Some possible burr appearances: from burr-free (left) to multilayered adhesion (right). Cutting direction from left to right.

dynamics that influence process efficiency and determine cut quality characteristics such as ripple (or striation) patterns and burr formation.[2–4]

Melt adhesion and subsequent burr formation take place when the internal inertia of the melt is insufficient to overcome the capillary forces at the bottom edge of the cut flank. To characterize the melt flow state with respect to burr formation, we use the liquid Weber number, as proposed in Refs. 5–7. The Weber number represents the ratio of the inertial forces in the melt and the capillary forces. It must be (sufficiently) higher than one for residue-free melt removal,

$$We = \frac{\rho_m v_m^2 d_m}{\sigma_m} > 1, \tag{1}$$

where ρ_m is the melt density, v_m the melt flow velocity, σ_m the melt surface tension, and d_m the melt film thickness. If the internal inertia drops and takes on comparable values to the capillary forces ($We \leq 1$), the melt is unlikely to detach from the workpiece, and the tendency to form burrs is high.

In the main flow direction (z), the melt is primarily accelerated by the shear force exerted by the gas jet. The momentum balance with the terms of gas inertia, gas pressure, and shear force can be written as[1]

$$\rho_g v_g \frac{dv_g}{dz} + \frac{dp_g}{dz} = -\frac{\tau_w}{r_c}, \tag{2}$$

where ρ_g, v_g, and p_g are the density, velocity, and pressure of the gas flow, τ_w is the wall shear stress, and r_c the cutting front radius (respectively, half kerf width). The shear-stress transfer on the melt surface can be derived from Newton's friction law for plane Couette flows.[1] In a cylindrical coordinate system, the shear stress on the melt τ_m is

$$\tau_m = \eta_m \frac{2v_{m,r}}{d_m} (= \tau_w), \tag{3}$$

where η_m is the melt viscosity and $v_{m,r}$ the radially averaged melt velocity in the z-direction. Equation (3) indicates that the flow velocity increases linearly with the melt film thickness for a given shear stress.

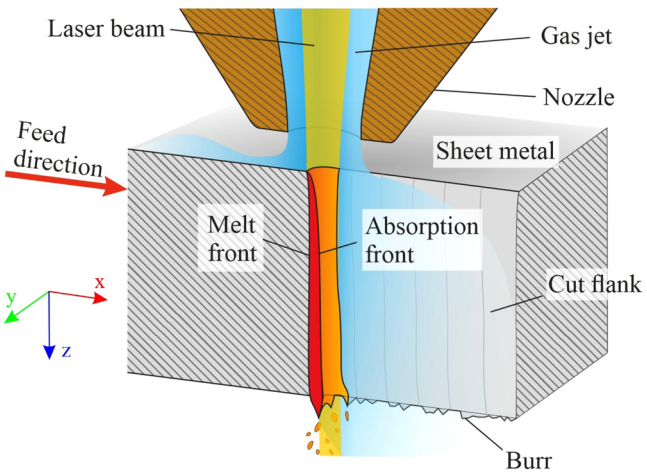

FIG. 2. Schematic representation of the laser cutting process and the boundary surfaces in the kerf. Cross section along the cutting direction.

In the azimuthal direction (with respect to the z axis), the melt surface tension σ_m causes a capillary pressure p_σ, directed toward the cutting front apex due to the lateral change of curvature,[1]

$$p_\sigma = \frac{\sigma_m}{r_c}. \tag{4}$$

When the melt surface temperature T_s reaches the vaporization temperature T_v, the capillary pressure p_σ is counteracted by the evaporation pressure p_v. At this point, a liquid–gas phase transition takes place in which mass, momentum, and energy density change abruptly. The evaporation is a nonequilibrium process characterized by a large energy consumption and a high increase in specific volume. Vaporization has a strong cooling effect on the melt due to the enthalpy of vaporization, which is an order of magnitude higher than the enthalpy of fusion in steel materials.[8] A detailed derivation of the mass and force balance of evaporation is given in Refs. 1 and 9. The vapor and the capillary pressure are taken into account in the azimuthal force balance by the pressure difference in the azimuthal direction p_φ,

$$p_\varphi = p_v(T_s) - p_\sigma(T_s) - p_a, \tag{5}$$

with p_a as the ambient pressure. It can be shown that p_φ becomes positive already a couple of 100 K below the boiling temperature (for typical radii of curvature r_c) and generates a lateral mass transport.[1]

The momentum contributions in the azimuthal direction cause a lateral melt flow that is distributed on the cut flank. The dynamics of the lateral mass flow decisively influence the formation and shape of the ripples on the cut flank.[2–4] The strength and distribution of the lateral flow also determine the amount of melt adhesion and the topology of solidification. A study conducted by Petring *et al.*[10] found a significant correlation between the relative amount of the calculated lateral mass flows and the measured burr lengths. In Ref. 7, the authors observed the melt ejection and characterized its dynamics. It was found that the melt removal rate increased when the melt flow was spatially compact and temporally stable. Furthermore, a specific characteristic of a burr-free process was a melt ejection that formed a threefold outflow, consisting of a front and two localized side flows (i. e. one side stream on each cut side). In addition, a liquid sheet was observed, which formed cyclically between the front and side flows. The conclusion drawn was that the localization of the side flow increased its thickness, and the liquid sheet refers to a nearly laminar melt current with a low Reynolds number. In the present study, we analyze the influence of the magnitude and distribution of vapor pressure gradients on the dynamics of the lateral mass flow, and subsequently, the burr formation. The structure of the study is outlined in Fig. 3.

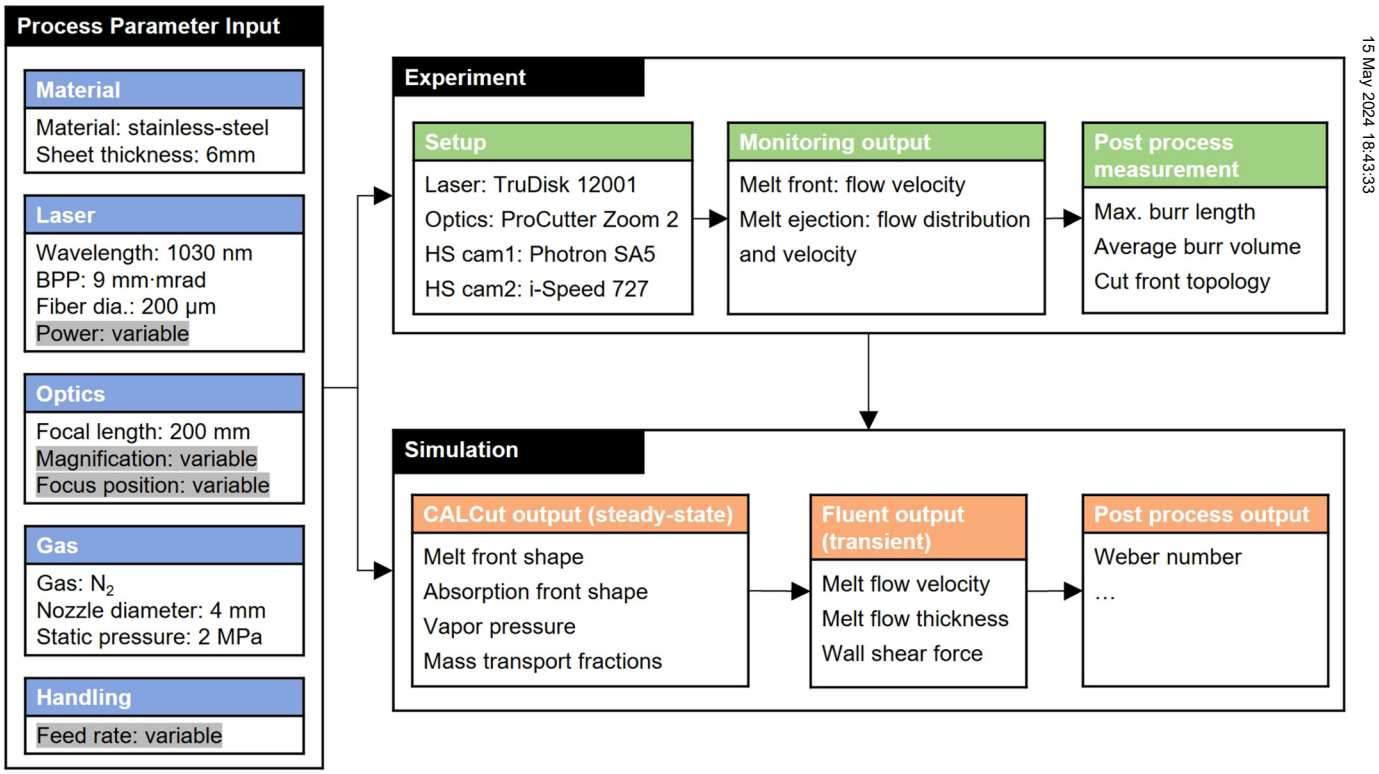

FIG. 3. Structure of the study, information flow, and output quantities.

TABLE I. Beam parameters as a function of magnification M.

M	w_0 (μm)	F-number	Z_R (mm)
1.5	150	8.3	2.5
2.0	200	11.1	4.4
2.5	250	13.9	6.9

II. EXPERIMENTAL SETUP

The investigation was conducted on a 6 mm stainless-steel sheet metal (1.4301). The main components of the experimental setup are a laser source of 1 μm radiation (TruDisk 12002, P_{nom}: 12 kW, BPP: 9 mm mrad, fiber diameter: 200 μm) and a processing head with variable optical magnification (Precitec ProCutter Zoom 2, focal length: 200 mm). The parameter variation includes variation of power (P), optical magnification (M), focus position, and cutting speed (v_c) (i.e. feed rate). Three laser power levels (6, 8, and 10 kW) and three magnification factors were tested. The magnification factors and their corresponding caustic parameters (waist radius w_0, F-number, and Rayleigh length Z_R) are listed in Table I.

The influence of the focus position was tested from 6 to −5.6 mm (with respect to the sheet surface) in seven steps. The cutting speed was varied starting from 1.6 m/min up to the separation limit at an increment of 0.4 m/min. The separation limit was resolved within ±0.1 m/min. The process gas was N_2, and the cutting nozzle was conical with an exit diameter of 4 mm. The static gas pressure was 20 bar. The clearance between the nozzle tip and the sheet surface was 0.7 mm.

The melt flow was observed *in situ* by two monochrome high-speed cameras: a "front camera," placed parallel to the cutting direction, and a "side camera," perpendicular to the cutting direction (see the sketch in Fig. 4). The front camera captures the melt flow along the cutting front, whereas the side camera captures the melt ejection below the sheet. The camera specifications and settings are listed in Table II. The recordings of both cameras were evaluated for an equivalent cut length of 15 mm, beginning at 2 mm after cutting started. The videos were processed with the open-source software FIJI.[11]

III. NUMERICAL INVESTIGATION

Numerical modeling is carried out in two steps. First, CALCut laser cutting simulation software was utilized to calculate absorption front and melt front geometry and important melt flow parameters such as melt film thickness, average melt surface temperature, vapor pressure gradients, and mass transport fractions for the selected samples. CALCut is based on a 3D steady-state model of the cutting process incorporating laser-beam absorption, heat conduction, phase transformations, and momentum transfer from the gas jet.[1,12] The precision and validity of CALCut's results have been tested and confirmed in a variety of studies for nearly 30 years. However, CALCut's spatial domain is parametrized by semi-cylindrical cutting front segments, allowing calculation of the melt flow up to the cutting front boundaries at the bottom edge and the transition to the flank. Further calculations along the flank as well as simulation of burr formation are not within the scope of CALCut (see Fig. 5).

In the second step, the numerical model was enhanced by a transient flow simulation. This simulation is conducted with Ansys Fluent, comprises an extended spatial domain, and uses the solution data obtained from CALCut as input.

A. Ansys CFD model

The fluid dynamics simulation (CFD) was implemented utilizing the simulation software ANSYS Fluent. The numerical model underwent systematic optimization, enabling efficient computations on a standard PC workstation (Intel Xeon W-2125, 32 GB RAM).

1. Simulation domain

The geometry of the CFD domain and its objects are depicted in Fig. 6. The two phases (N_2 gas and stainless-steel melt) enter the domain through corresponding inlets. The gas inlet is on the top of the pressure chamber and is placed 25 mm above the nozzle orifice. The shape of the melt inlet corresponds to the melting front calculated by CALCut. The cut flanks are extruded from the lateral boundary of the melt inlet. The geometry of the nozzle corresponds to the one used in the experiment. The distance from the interaction zone to the outer limits of the domain (pressure outlet) is large enough to allow full development of the flow. The outer dimensions of the domain are $70 \times 70 \times 30$ mm^3 (H × W × D).

2. CFD mesh

The finest resolution of the initial mesh is in the vicinity of the cutting front with an edge length of 40 μm. During solution, automatic mesh adaptation is used to reduce the length of the cell within the liquid phase down to 10 μm. The automatic mesh adaptation drastically increased the level of detail of the melt flow, while only moderately increasing the total number of cells, from initially around 280 000 cells to approximately 360 000 (the numbers vary slightly from case to case). The mesh topology in the vicinity of the kerf entrance is shown in Fig. 7.

The orthogonal quality of the mesh in all presented cases is higher than 0.2. The value of y+ is well below 100 in the region of

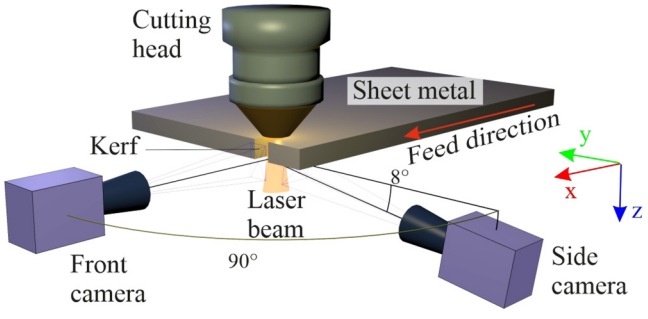

FIG. 4. Camera arrangement.

TABLE II. Camera specifications.

	Front camera	Side camera
Type	Fastcam SA5	i-Speed 727
Acquisition rate	100×10^3 fps	150×10^3 fps
Video resolution	128×376	500×310
Spatial resolution	20 μm/pixel	13 μm/pixel

interest. The resulting flow Courant number is smaller than 5, with the maximum value being reached in the area above the melt. These values are considered appropriate to promote the stable behavior of the numerical solution.

3. Solver

Since we were interested in the dynamics of the flow, the fluent solver was used with transient time formulation. For the two-phase model, two materials were defined: nitrogen gas (N_2) and stainless-steel melt. The pressure inlet of the gas flow is set to 2 MPa. The melt enters the domain at a velocity equal to the cutting speed. The melt inlet temperature is equal to the average melt temperature calculated by CALCut. The material properties of the stainless melt are listed in Table III. Phase transitions are neglected.

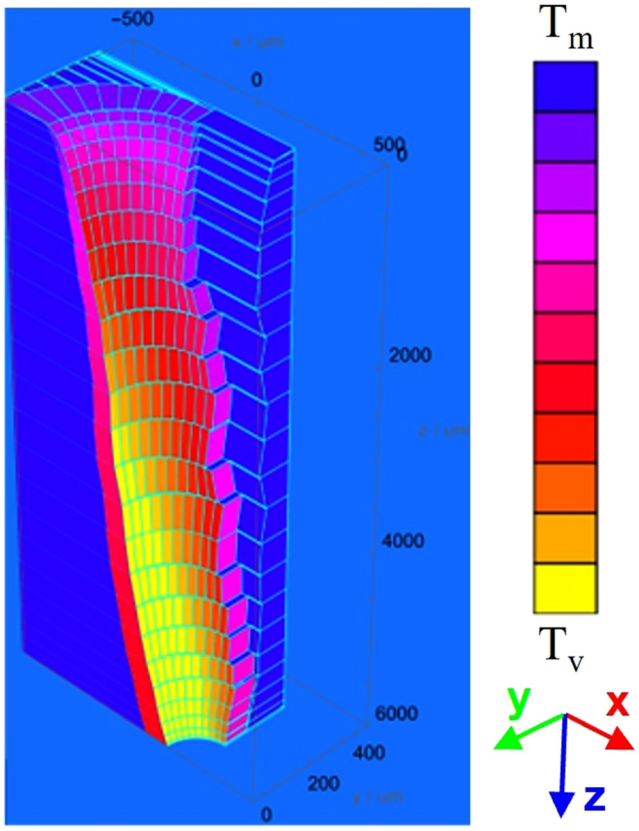

FIG. 5. CALCut calculation of absorption front geometry, melt film thickness, and surface temperature in the case of the nearly burr-less sample No. 141 (see Table IV).

The multiphase model used is the volume-of-fluid (VOF) model. In the VOF model, only one set of momentum equations is shared by all phases, and the phase interface is determined by tracking the volume fractions of the phases. However, the location of the interphase is smeared within the cell volume, so the accuracy of the model depends strongly on the mesh resolution.[17–20] In this study, the interphase is set to a volume fraction (VF_m) of 0.5 (see Fig. 8). The VOF model was chosen as it consumes fewer computational resources than the more sophisticated Eulerian model, which is easier to set and more stable in the present configuration.

To account for the adhesion forces acting on the melt along the contact line with the solid kerf walls, the VOF model requires the input of the contact angle. Liquid metals flowing over the substrate of the same material are usually highly wettable.[21,22] The high surface energy of the melt results in contact angles at the triple line (i.e. the line where the three phases: solid, liquid, and gaseous, are in contact) considerably smaller than 90°. By comparing our results with values from the literature[21–23] and measurement of the resolidified burrs, we estimated the average contact angle to be 65°.

The viscous model used is shear-stress transport k-omega with compressibility.

To account for the effect of the evaporation pressure, a custom volumetric momentum source is defined, which acts on the surface of the melt phase. A momentum source in Fluent adds a volumetric body force F in the momentum conservation equation to be solved,[19]

$$\frac{\partial}{\partial t}(\rho\vec{v}) + \nabla(\rho\vec{v}\cdot\vec{v}) = -\nabla p + \nabla\cdot(\bar{\bar{\tau}}) + \vec{F}, \tag{6}$$

where p is the static pressure, $\bar{\bar{\tau}}$ the stress tensor, and $\vec{F}$ an external volumetric force with the unit N/m^3. To simulate the lateral acceleration due to the vapor pressure gradients, we approximated the lateral components of F as follows:

$$F_x(z) = -F_y(z) = \frac{p_v(z)}{l_v}, \tag{7}$$

where p_v is the vapor pressure and l_v the effective length at which the vapor pressure relaxes to ambient level. In the z-direction, we assumed a polynomial dependency of the vapor pressure $p_v(z)$. To approximate p_v, we used the average vapor pressure in the kerf $\overline{p_v}$ as well as the vapor pressure on the bottom edge $p_{v,b}$ calculated by CALCut. With $p_v(z_0) = 0$ on the upper edge z_0 and $p_v(z_b) = p_{v,b}$

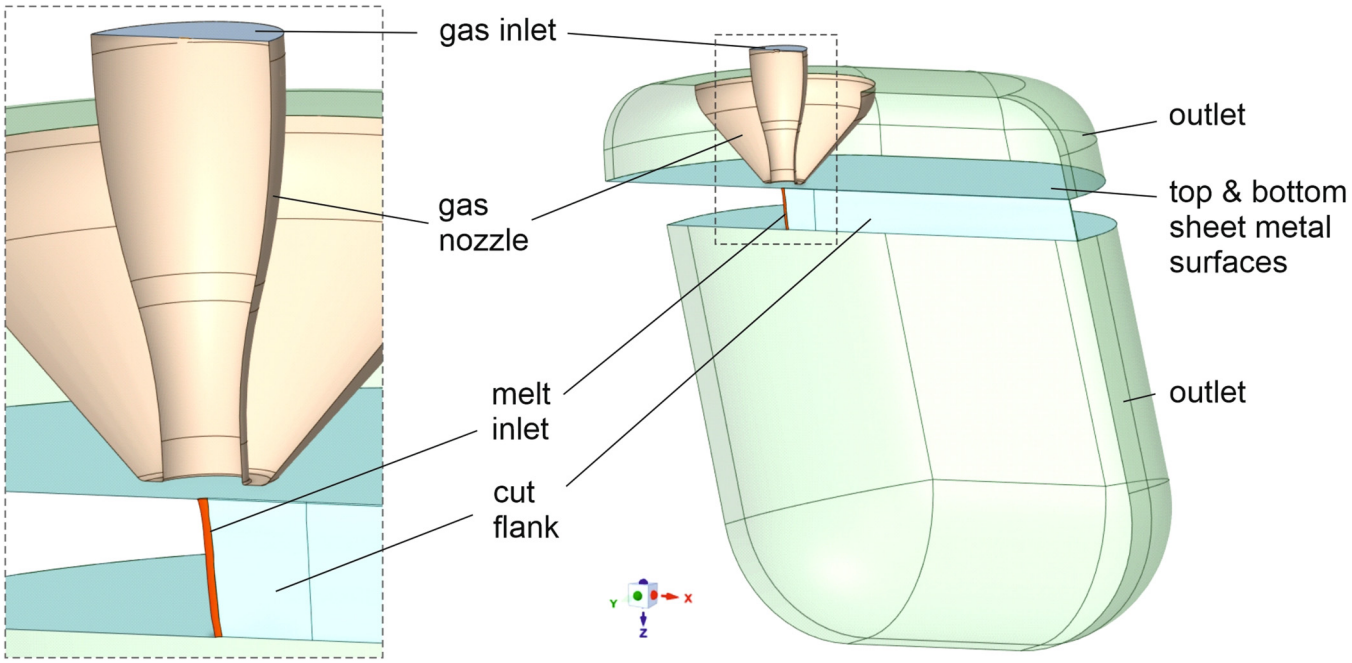

FIG. 6. CFD domain. The symmetry plane (the front face in this perspective) is transparent to allow better viewing.

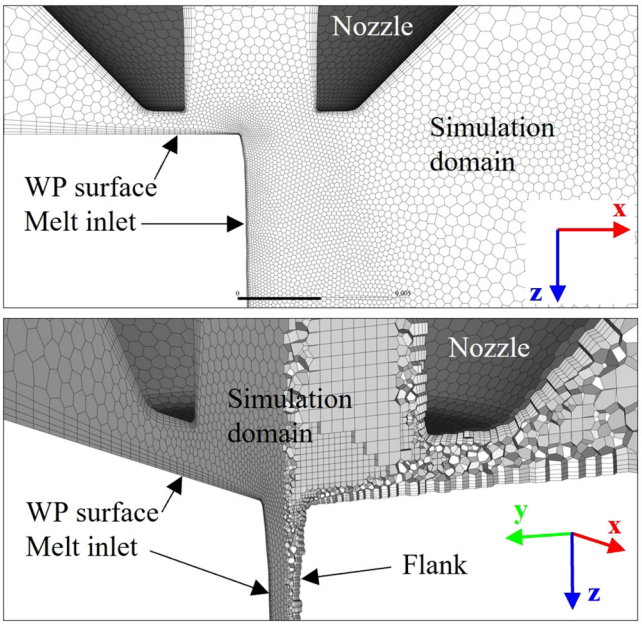

FIG. 7. CFD mesh. Top: section of the surface mesh on the symmetry plane in the region of the kerf entry; bottom: cross section through the volume mesh (work piece).

on the bottom edge z_b, we obtain the following expression:

$$p_v(z) = p_{v,b}\left(\frac{z}{z_b}\right)^n, \qquad n = \frac{p_{v,b}}{\overline{p_v}} - 1. \tag{8}$$

The effective relaxation length l_v from Eq. (7) was empirically adjusted using the melt flow video recordings from the experiment.

TABLE III. Material properties of liquid stainless steel. The values originate from Refs. 13–16.

Property	Symbol	Value
Density	ρ	6490 kg/m^3
Specific heat	c_p	835 J/(kg K)
Thermal conductivity	κ	40 W/(m K)
Melting temperature	T_m	1712 K
Viscosity	η_m	$\eta_{m0} \times \exp\left(\frac{E}{RT_m}\right)$
	η_{m0}	3.699×10^4 kg/(m s)
	E	4.14 J mol
	R	8.314 J/(mol K)
Surface tension	σ_m	$\sigma_{m0} + (T - T_m)\left(\frac{d\sigma_m}{dT}\right)$
	σ_{m0}	1.6 N/m
	$\frac{d\sigma_m}{dT}$	-0.52×10^{-3} N/(m K)

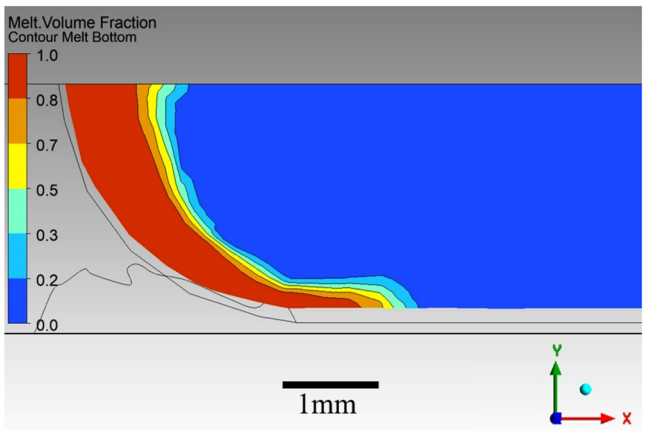

FIG. 8. Example of the melt volume fraction cross-distribution. Cross section on the exit of the cut kerf.

The most consistent results were achieved for l_v equal to twice the average melt front radius (i.e. average kerf width): $l_v = 2r_m$.

The expression in Eq. (7) takes into account the way the momentum source is defined in Ansys by means of Cartesian coordinates. The momentum source is limited to apply solely on the melt "surface" with $0.3 < VF_m < 0.7$ (cf. Figure 8). As the melt flow is confined by the semicircular melt front and the kerf wall, $\vec{F}$ induces an azimuthal motion along the melt front and a linear motion in the x-direction along the flank.

Furthermore, we used a pressure-based solver with SIMPLEC pressure–velocity coupling, a second-order upwind discretization scheme, and a bounded second-order implicit transient formulation (see Ref. 19 for details). The time step was set to 0.5 μs and the total number of time steps was 10 000 (flow time 5 ms). The simulation was evaluated within the time range of 2–5 ms to ensure that the two-phase flow is fully developed and reached a quasistationary state. Solution data were exported every 5 μs.

Subsequently, the results of the numerical simulation were experimentally verified. A schlieren image of the gas flow within a kerf model was compared to a one-phase gas flow over the same geometrical configuration. The comparison can be seen in Fig. 9. The supersonic structures developing within and below the cut channel show good agreement, which is an indication that the density gradient and flow velocity are calculated correctly.

As an example, a comparison of the melt wave dynamics at the cutting front apex is made using streak imaging[24] and shown in Fig. 10. The identical slope of the streaks indicates that the wave speed is identical and melt dynamics are generally well reproduced.

The distribution of the measured maximum burr lengths (BL_{max}) for the present configuration of laser, optics, and workpiece is shown in Fig. 11. An overview of the samples selected for further investigation with input parameters, cut quality, as well as numerical solution quantities is listed in Table IV.

IV. RESULTS AND DISCUSSION

The maximum burr length (BL_{max}) and flank roughness ($R_{z,max}$) were measured to determine the cut quality. As an overview of the cutting tests performed, we plotted BL_{max} as a function of the cutting speed and focus position for constants P and M,

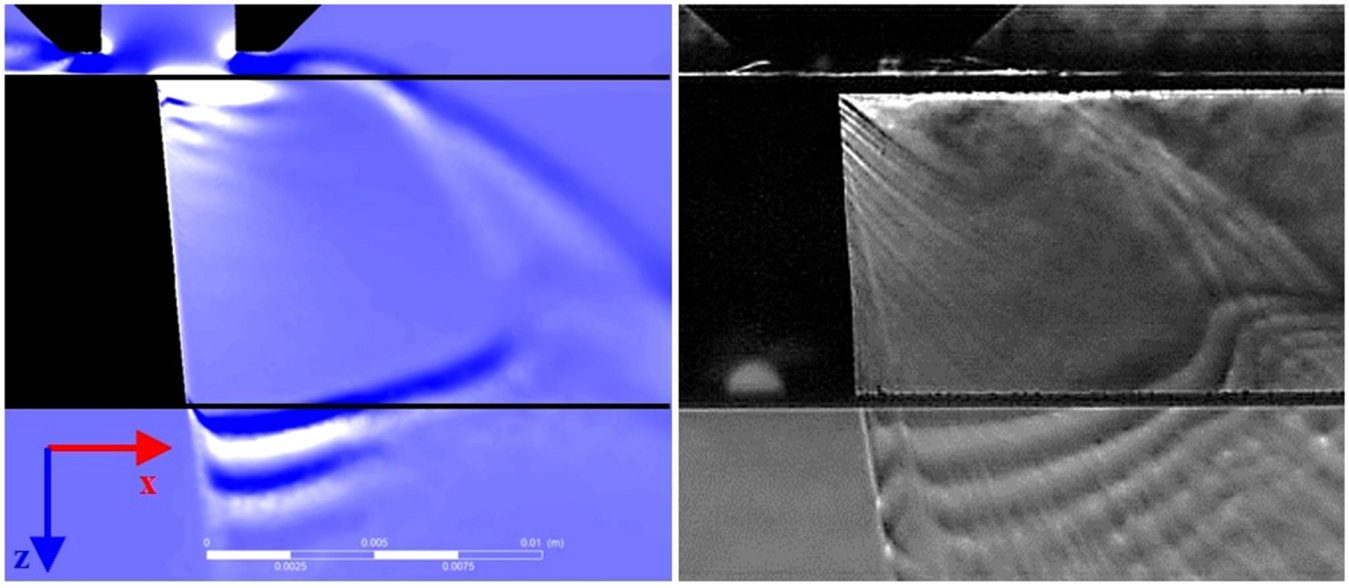

FIG. 9. Comparison of the gas-flow simulation (left) with a schlieren image (right) of an identical kerf model made of glass. The colors correspond to the magnitude of the density gradients. "Sheet thickness" is 10 mm, gas pressure is 20 bar, and nozzle diameter is 5 mm.

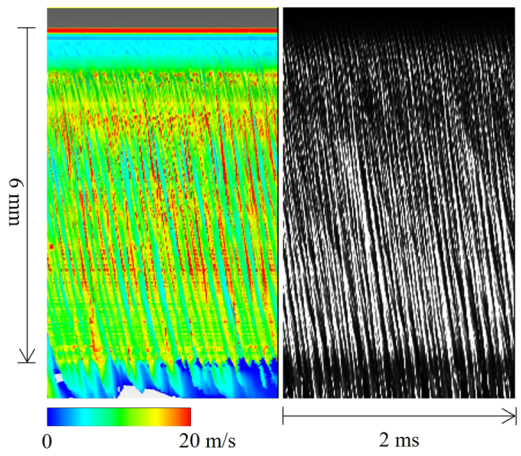

FIG. 10. Streak images of the calculated and recorded melt wave dynamics, an example shown for sample No. 24 (see Table IV).

respectively, as shown in Fig. 11. The samples used in the presented numerical investigation are marked with circles.

According to the burr length measurements in Fig. 11, the least dross is formed in the middle of each process subdomain of constant power and magnification. A minimum $BL_{max} = 21\,\mu$m was determined for $P = 10$ kW, $M = 2$, $z_f = -1.4$ mm, and $v_c = 4$ m/min (sample No. 281).

The second and third best cuts, Nos. 24 and 141, were generated with the same caustic settings, slightly lower speed (3.6 m/min) and lower power, 6 and 8 kW, respectively. The appearance of the cut flanks is quite similar, as shown in Fig. 12. The burr is a thin, uniform seam with few melt accumulations.

The *in situ* videography of the melt ejection shows that a triple melt outflow forms at parameter No. 24, similar although not as pronounced to that described in Ref. 7. However, the separation of the flow gradually disappears as the power increases, and the expulsion merges into a coherent, compact flow, as can be seen in Fig. 13. The fluent results show that the CFD model can resolve the threefold separation of the flow in essence, but not as pronounced as observed experimentally (see Fig. 14, top). CALCut determines a

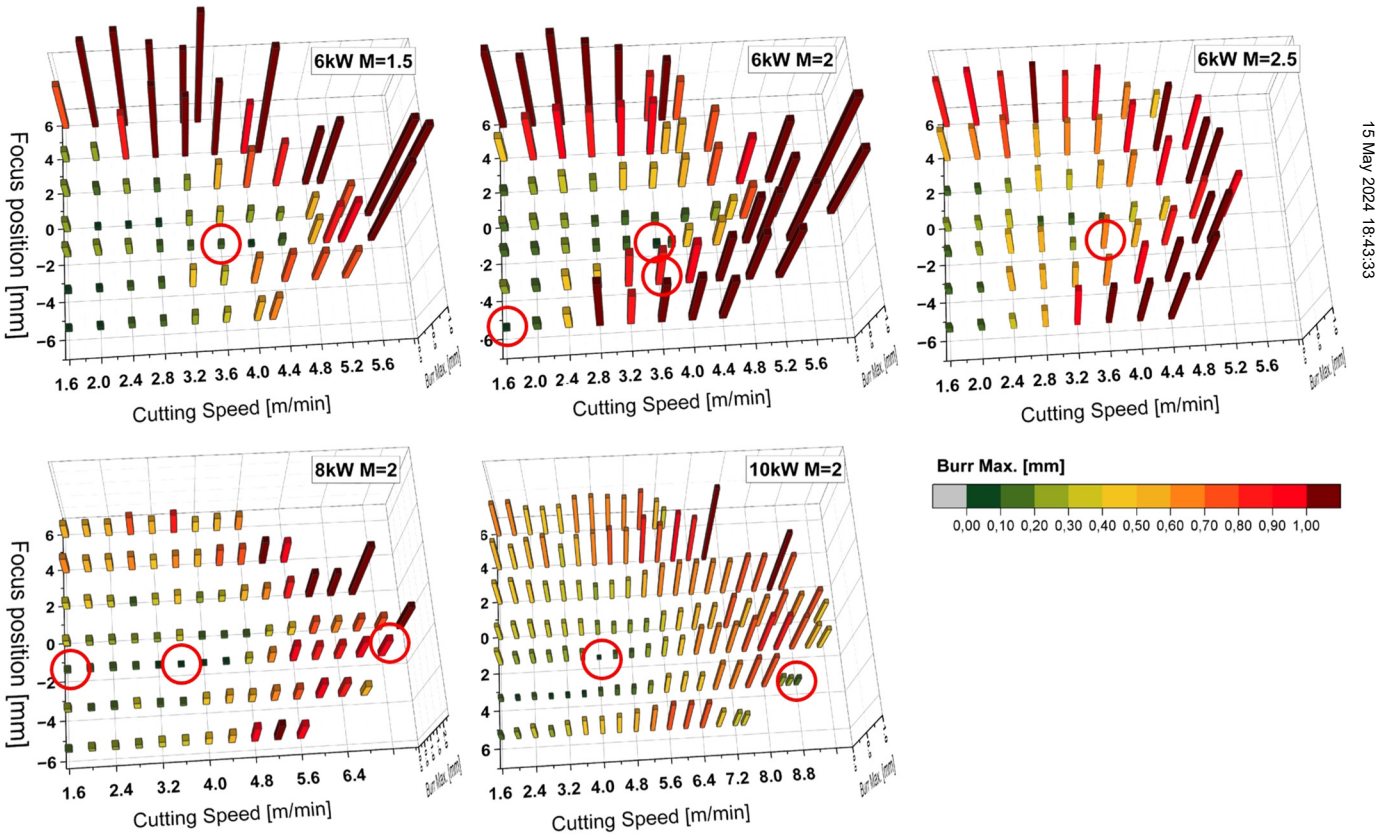

FIG. 11. Summarized measurement of the maximum burr length plotted against cutting speed and focus position for different power levels and magnification settings. Parameters used in the CFD are marked with circles.

TABLE IV. Selected samples, their input parameters, quality values, and solution variables.

Sample No.	M	P (kW)	Z_f (mm)	v_c (m/min)	Burr max. (μm)	$R_{z,\max}$(μm)	Avg. vapor pressure (bar)	Vapor pressure bottom edge (bar)	Lateral mass transport (%)	Mass transport vapor (%)	We avg.	We std.
24	2	6	−1.4	3.6	38	19	0.3	1.5	37.9	4.8	23.5	28.71
42	2	6	−3.4	3.6	858	86	0.4	1.4	37.6	5.3	25.8	21.67
54	2	6	−5.4	1.6	48	55	0	0	18.7	0.1	10.24	8.81
136	2	8	−1.4	1.6	117	41	0	0	18.8	0	6.84	7.86
141	2	8	−1.4	3.6	26	25	0.4	1.3	37.7	6	34.46	38.24
149	2	8	−1.4	6.8	925	45	1.1	1.4	85.5	9.5	14.18	16.46
281	2	10	−1.4	4	21	23	0.6	1.3	52.6	8.4	17.18	6.48
318	2	10	−3.4	8.8	188	65	1.2	2.3	88.1	8.8	19.04	24.57
442	2.5	6	−1.4	3.6	695	26	0.4	3.3	58.9	6	18.88	4.3
540	1.5	6	−1.4	3.6	111	21	0.3	1.4	38.2	4.9	24.14	25.89

moderate lateral mass flow of about 40%–50% for the three sample Nos. 24, 141, and 281.

When the outflow velocity $v_{m,b}$ and thickness $d_{m,b}$ are evaluated at the bottom edge of the cut flank, a position-dependent Weber number can be given, averaged over the calculated flow time of 3 ms. Within this time, 600 time steps are stored and, therefore, enough values $We_i(x, t)$ are available for sufficient statistics. Furthermore, with an average melt flow speed in the order of 10 m/s, this period is several times greater than the time constant of the melt removal (0.6 ms). Additionally, the acquired Weber number We_i values were distributed into four value ranges (0–1, 1–5, 5–50, and >50) and their relative occurrence over time[25] was plotted along the bottom flank edge (x-direction).

For the three samples, the Weber number has values significantly higher than one over the entire lateral extension of the flow; an example is shown for sample No. 281 in Fig. 15. Toward the triple line on the flank (melt flow boundary in the x-direction) at $x = 0.64$ mm, the melt film thickness decreases, but the flow remains compact and its velocity high. The higher standard deviation reflects the higher flow irregularity there.

In the presence of strong lateral flow components, the Weber number increasingly falls near the triple line. This can be clearly seen in the case of sample No. 149. This cut was produced at a high cutting speed (6.8 m/min), close to the separation limit, and has $BL_{\max} = 952\,\mu$m. According to the calculation, the predominant part of the melt is expelled into the front half of the flow, and the Weber number is high, as shown in Fig. 16. Toward the flow boundary, 2 mm behind the main axis, the Weber number drops considerably below one. This part of the flow is the main contributor to the burr formation.

At 1.1 bar, the mean vapor pressure in the kerf is one of the strongest in the test field (cf. Table IV). This drives parts of the melt far back along the flank, as can be seen in Fig. 17.

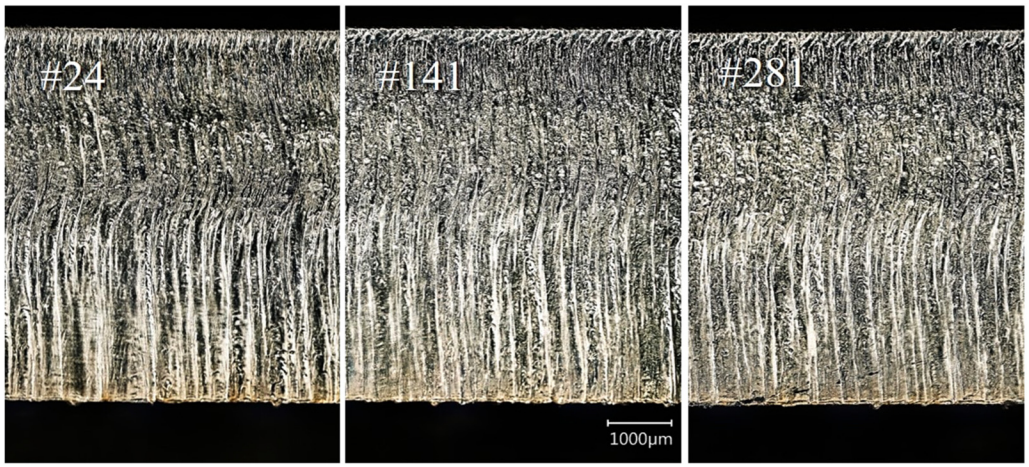

FIG. 12. Cut flanks, sample Nos. 24, 141, and 281. The cutting direction from left to right.

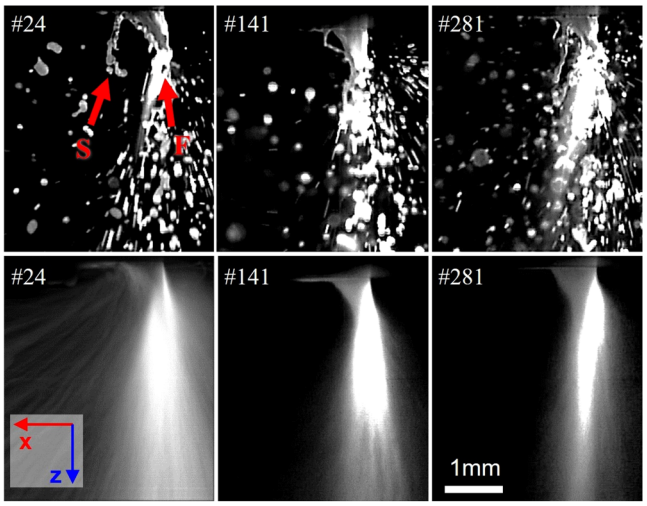

FIG. 13. Single frames (top) and average over 2000 frames (bottom) of three samples (Nos. 24, 141, and 281) with increasing power (6, 8, and 10 kW). Front (F) and side flows (from both flanks) (S) of No. 24 are marked.

In the process, the current is broken up and flows as strands and droplets along the flank. Due to their high wettability, the melt droplets spread out and cannot be sufficiently accelerated by the gas jet. As a result, the Weber number in the rear third of the flow drops below one and a pronounced burr forms. This is consistent with the observation of the outflow shown in Fig. 18. Here, it is also evident that burr is deposited only after the main flow and gradually grows over several millimeters along the bottom edge.

As the cutting speed is increased toward the separation limit, the burr length generally increases as well (cf. Figure 11), a direct consequence of the increased melt volume-flow that must be ejected from the kerf. An interesting exception here is the parameter group, including sample No. 318 at 10 kW power, a focus position of −3.4 mm, and cutting speed $v_c > 8.4$ m/min (bottom right corner in Fig. 11). Here, the trend is reversed, and the burr length decreases significantly, shortly before the cutting speed reaches the separation limit at 8.9 m/min. The effect is reproducible and can also be seen to some extent with other focal positions at 10 kW.

According to the investigation conducted using CALCut, the cutting limit should have been reached at a speed of 7.6 m/min, based on the power level and focus position employed. This suggests the presence of a high-temperature effect that is not accounted for in the calculation. The ripple pattern of the cut flank, as depicted in Fig. 19 (top), reveals that the upper half of the cut front exhibits a significant backward tilt. This phenomenon is commonly observed shortly before the cutting process terminates due to insufficient energy input.[26] In contrast, the lower half of the cut flank exhibits a more erratic appearance, characterized by significant splatter and recast. Process monitoring using the front camera reveals a notable increase in process emission within the

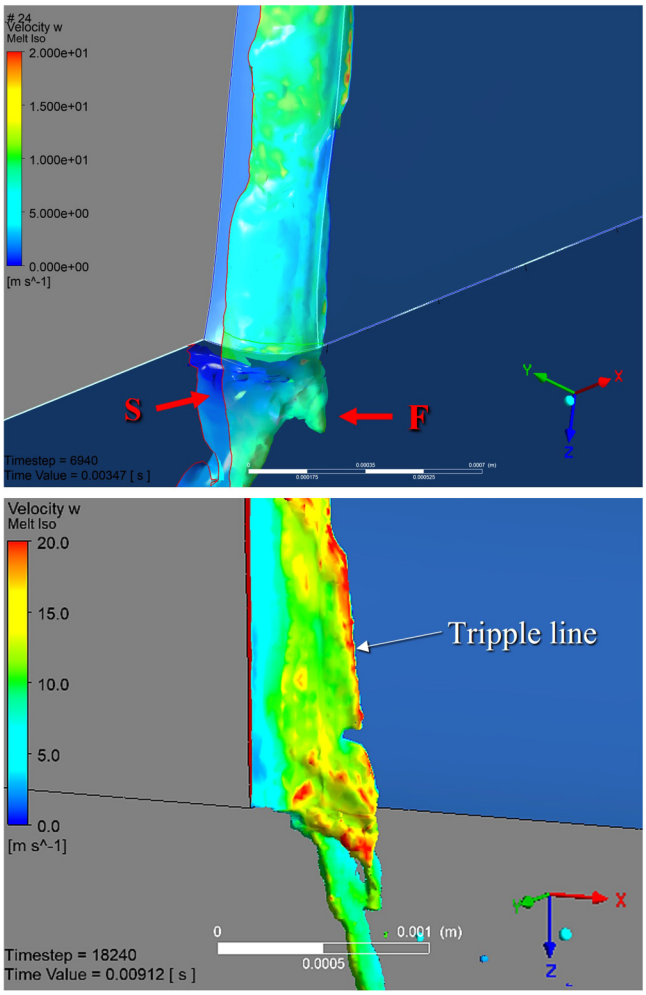

FIG. 14. CFD of the melt flow over the bottom kerf edge, No. 24 (top), and No. 281 (bottom). Front (F) and side flows (S) of No. 24 are marked.

center kerf region, as depicted in Fig. 19 (bottom left). The side camera images show a fast and compact melt expulsion, accompanied by a persistent vapor trail (visible as a bright blurred trace in Fig. 19, bottom right). The CALCut calculation performed at a lower speed of 7.6 m/min yielded an average vapor pressure of 1.2 bar and vapor pressure on the bottom edge of 2.3 bar: in total, the highest values within the test field.

These observations suggest that metal vapor recondenses at midcutting depth, with energy being recoupled into the melt flow through the enthalpy of condensation. In the CALCut model, the metal vapor is assumed to flow out of the domain, and the enthalpy of vaporization stored within it is treated as an energy loss. Here, the specific shape of the cut front prevents the vapor from effectively escaping out of the interaction zone. In addition, there is an increased level of beam absorption by the metal vapor, which intensifies the condensation process as the current density of

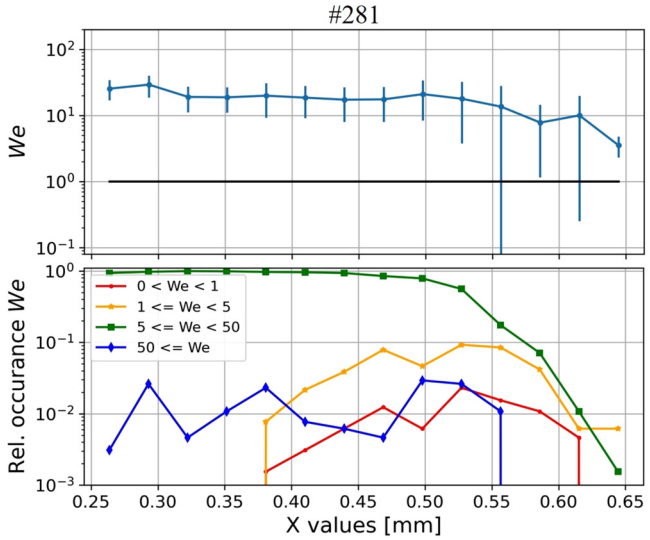

FIG. 15. Weber number (top) and its relative occurrence (bottom) along the lower edge of the cut flank on No. 281 (x = 0 refers to the beam axis).

condensing particles rises with the vapor temperature.[27] Obviously, this phenomenon primarily takes effect at very high evaporation rates, where the proportion of recondensing vapor particles becomes significantly high so that it influences the overall dynamics of the cutting process. The reintroduced enthalpy increases the fusion rate on the melt front and restarts the abrasion process,

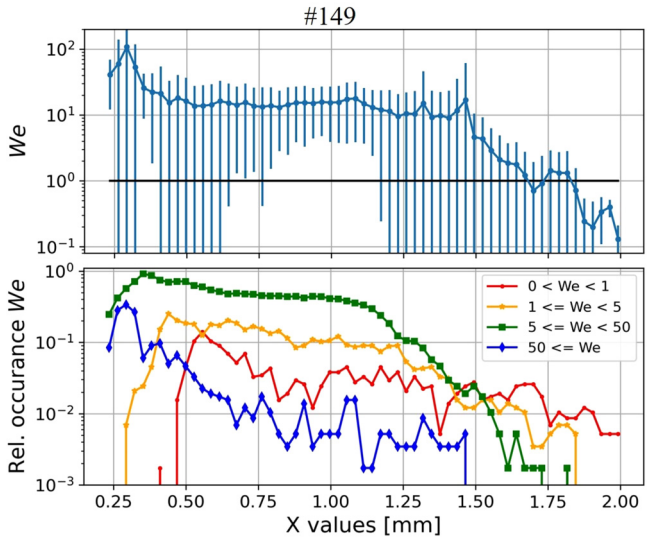

FIG. 16. Weber number (top) and its relative occurrence (bottom) along the lower edge of the cut flank on No 149.

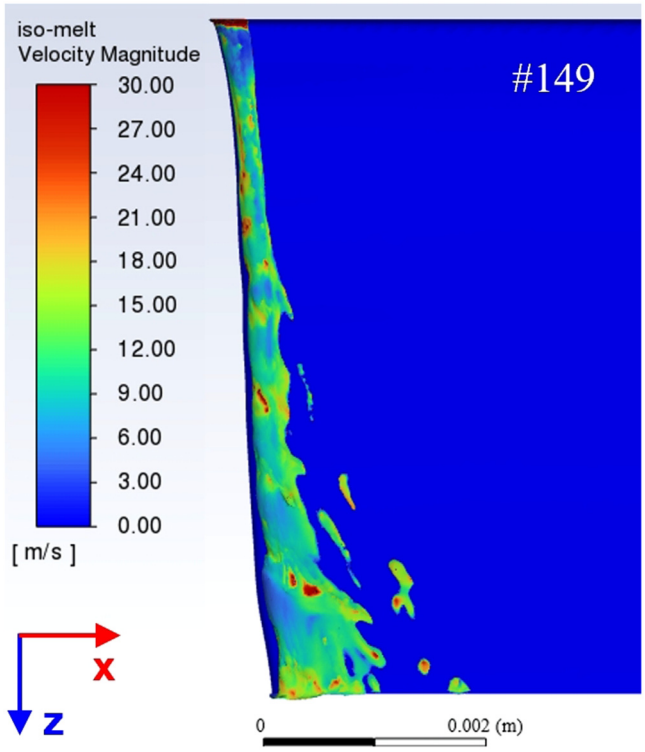

FIG. 17. Simulated distribution and velocity of the melt flow for No. 149.

increasing the cutting limit beyond the model prediction. The low focus position favors the coupling of energy further down the kerf. As a result, the very hot and highly fluid melt can be effectively expelled through the gas jet, resulting in a minimal melt attachment.

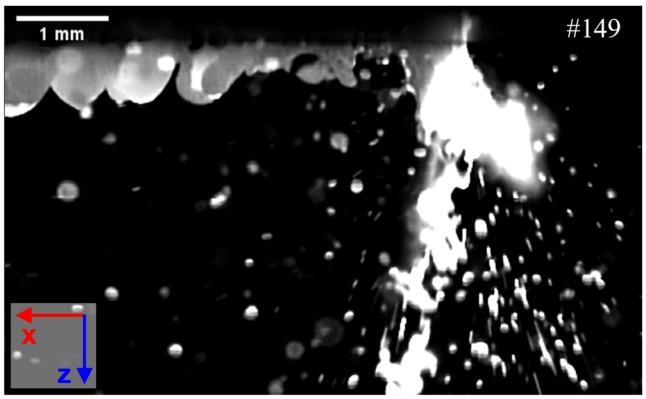

FIG. 18. Melt outflow of No. 149 as observed by the side camera.

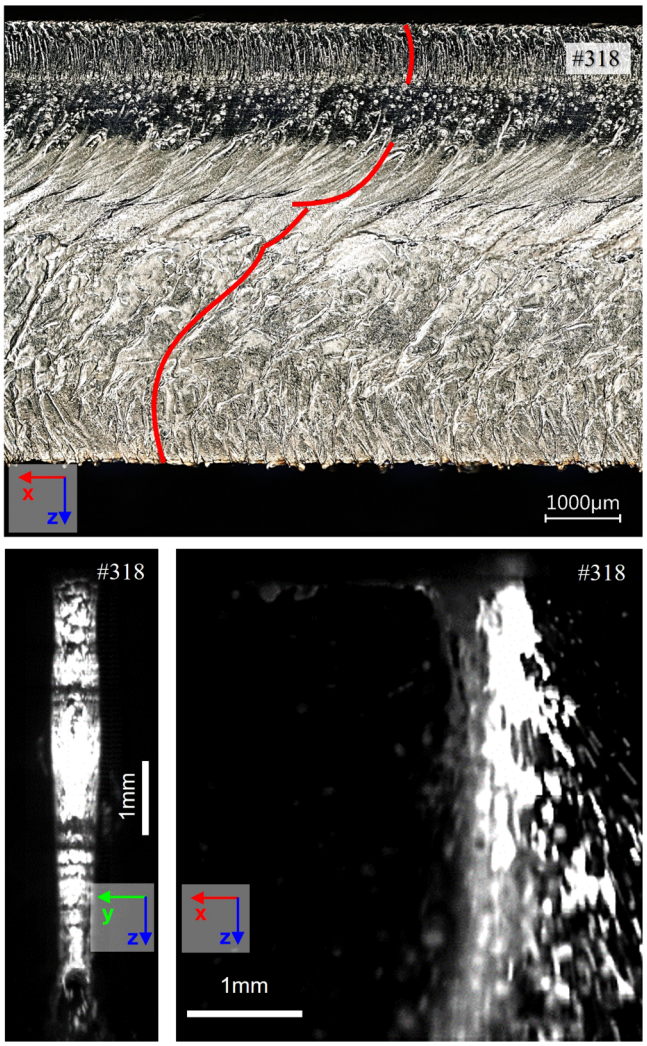

FIG. 19. Cut flank of No. 318 (top) with the characteristic ripple pattern (red line), as well as single frames from the front (bottom left) and side camera (bottom right).

V. CONCLUSIONS

In the present study, we investigated melt ejection and burr formation during laser-beam cutting, both experimentally and numerically. Based on the observations, the following conclusions can be made.

The Weber number serves as a useful metric for assessing the tendency of burr formation. However, it is important to consider its distribution along the bottom edge, as mean values alone do not exhibit a clear correlation with the burr length.

The results suggest that the melt flow properties in the vicinity of the triple line on the cut flank primarily contribute to burr formation.

Burr formation is promoted by a locally low Weber number near the triple line, even if the rest of the flow has high Weber numbers, which locally leads to efficient melting.

The three best cuts in the test field in terms of the burr length have similarly high vapor pressures, $\overline{p_v} \approx 0.5\,\mathrm{bar}$ and $p_{v,b} \approx 1.3\,\mathrm{bar}$, and have moderate lateral flow fractions of around 50%. The melt flow is compact, and the triple line along the flank is regular. The threefold distribution of the melt flow, which was associated with residual-free melt separation in Ref. 7, could be confirmed. However, the splitting tends to occur at moderate power levels (here, 6 kW) and disappears when the power is increased, while the Weber number values of the flow remain high.

Moderate burr formation is mainly influenced by flow instabilities, such as wave overlap, wave breaking, and localized explosive evaporation.

Large burr formation can be attributed to high vapor pressures, which considerably accelerate the lateral flow of the molten material, ultimately causing its rupture. As a result, droplets and strands are formed, which possess longer triple lines. Due to the high wettability of the melt, their film thickness and, thus, Weber number are inevitably reduced.

At higher power levels, we observed a noticeable departure from the typical trend of increasing burr length as the velocity approaches the cutting limit. In the provided configuration, the burr length is reduced significantly near the cutting limit when a 10 kW power setting is used and the focus is positioned in the lower part of the sheet. This phenomenon is attributed to the recondensation of vapor particles because of very high evaporation rates and vapor pressures in the kerf. This reintroduces stored evaporation enthalpy into the melt flow, thus enhancing abrasion and melt removal. When this mechanism is cultivated, a new high-speed process window can be established for laser cutting in the thick section range, thus further expanding the capabilities and possibilities in this domain.

ACKNOWLEDGMENTS

The present study was conducted within the Cluster of Excellence "Internet of Production," Project-ID: 390621612 at the Fraunhofer Institute for Laser Technology ILT and complementarily in the context of the Collaborative Research Centre SFB1120-236616214 "Precision Melt Engineering" at the Chair of Laser Technology LLT of RWTH Aachen University, both funded by the German Research Foundation (DFG). The authors wish to express their sincere gratitude for the sponsorship and support.

AUTHOR DECLARATIONS

Conflict of Interest

The authors have no conflicts to disclose.

Author Contributions

S. Stoyanov: Conceptualization (equal); Data curation (equal); Formal analysis (equal); Funding acquisition (equal); Investigation (equal); Methodology (equal); Project administration (equal); Resources (equal); Software (equal); Supervision (equal); Validation (equal); Visualization (equal); Writing – original draft

(equal). **D. Petring:** Conceptualization (equal); Data curation (equal); Funding acquisition (equal); Methodology (equal); Project administration (equal); Resources (equal); Software (equal); Supervision (equal); Validation (equal); Writing – review & editing (equal). **F. Piedboeuf:** Data curation (equal); Formal analysis (equal). **M. Lopes:** Writing – review & editing (equal). **F. Schneider:** Project administration (equal); Resources (equal); Supervision (equal); Validation (equal); Writing – review & editing (equal).

REFERENCES

[1]D. Petring, "Anwendungsorientierte Modellierung des Laserstrahlschneidens zur rechnergestützten Prozeßoptimierung," Zugl.: Aachen, Techn. Hochsch., Diss: 1994 (Berichte aus der Lasertechnik), Shaker, 1995.

[2]D. Arntz-Schroeder and D. Petring, "Analyzing the dynamics of the laser beam cutting process," PhotonicsViews **17**, 43–47 (2020).

[3]K. Hirano and R. Fabbro, "Experimental investigation of hydrodynamics of melt layer during laser cutting of steel," J. Phys. D: Appl. Phys. **44**, 105502 (2011).

[4]D. Arntz, D. Petring, F. Schneider, and R. Poprawe, "In situ high speed diagnosis—A quantitative analysis of melt flow dynamics inside cutting kerfs during laser fusion cutting with 1 µm wavelength," J. Laser Appl. **31**, 22206 (2019).

[5]W. Schulz, V. Kostrykin, M. Niessen, J. Michel, D. Petring, E. W. Kreutz, and R. Poprawe, "Dynamics of ripple formation and melt flow in laser beam cutting," J. Phys. D: Appl. Phys. **32**, 1219–1228 (1999).

[6]U. Halm, "Simulation hochdynamischer vorgänge in der schmelze beim laserstrahlschneiden," Dr. Rer. Nat. dissertation, RWTH Aachen, 2018.

[7]S. Stoyanov, D. Petring, D. Arntz-Schroeder, M. Günder, A. Gillner, and R. Poprawe, "Investigation on the melt ejection and burr formation during laser fusion cutting of stainless steel," J. Laser Appl. **32**, 22068 (2020).

[8]M. Bober, and J. Singer, "High temperature vapor pressures of stainless steel type 14970 and of some other pure metals from laser evaporation," KFK–3772, 1984.

[9]M. Aden, E. Beyer, G. Herziger, and H. Kunze, "Laser-induced vaporization of a metal surface," J. Phys. D: Appl. Phys. **25**, 57–65 (1992).

[10]D. Petring, D. Arntz, S. Stoyanov, and F Schneider, "Effects of beam power and power density distribution on process and quality issues during fiber laser cutting of stainless steel sheet metal," in *Lasers in Manufacturing Conference*, Munich, 24–27 June 2019 [German Scientific Laser Society (WLT e.V.), Hannover, Germany, 2019].

[11]J. Schindelin, I. Arganda-Carreras, E. Frise *et al.*, "Fiji: An open-source platform for biological-image analysis," Nat. Methods **9**, 676–682 (2012).

[12]D. Petring, "Computer simulation of laser cutting for the limiting-value-oriented development of robust processes," Weld. Cut. **57**, 37–42 (2005).

[13]M. Beutl, G. Pottlacher, and H. Jger, "Thermophysical properties of liquid iron," Int. J. Thermophys. **15**, 1323–1331 (1994).

[14]C. J. Smithells, *Smithells Metals Reference Book*, 8th ed. (Elsevier Butterworth-Heinemann, Amsterdam, 2004).

[15]L. Battezzati and A. L. Greer, "The viscosity of liquid metals and alloys," Acta Metallurgica **37**, 1791–1802 (1989).

[16]B. J. Keene, "Review of data for the surface tension of pure metals," Int. Mater. Rev. **38**, 157–192 (1993).

[17]C. Hirt and B. Nichols, "Volume of fluid (VOF) method for the dynamics of free boundaries," J. Comput. Phys. **39**, 201–225 (1981).

[18]O. Ubbink and R. I. Issa, "A method for capturing sharp fluid interfaces on arbitrary meshes," J. Comput. Phys. **153**, 26–50 (1999).

[19]Ansys Fluent Theory Guide, *Ansys Fluent Theory Guide: Release 2021 R2* [German Scientific Laser Society (WLT e.V.), Hannover, Germany, 2021].

[20]N. D. Katopodes, "Volume of fluid method," in *Free-Surface Flow* (Elsevier, 2019), pp. 766–802.

[21]N. Eustathopoulos, "Wetting by liquid metals—Application in materials processing: The contribution of the grenoble group," Metals **5**, 350–370 (2015).

[22]N. Eustathopoulos, B. Drevet, and M. G. Nicholas, *Wettability at High Temperatures*, 1st ed., Pergamon Materials Series, Vol. 3 (Pergamon, Amsterdam, 1999).

[23]F. G. Yost and A. D. Romig, "Thermodynamics of wetting by liquid metals," MRS Proc. **108** (1987).

[24]To create a streak image, pixel stripes are extracted from the same location of subsequent video frames and arranged next to each other, thus creating a projection of the motion pattern over the time: "streaks" (see also Ref. 4, where this technique has been widely used to analyze melt wave dynamics in the kerf).

[25]This metric indicates the frequency of Weber numbers along the bottom edge within a given range of values and is normalized to the number of time steps. Not all time steps yield a Weber number due to interruptions in melt outflow.

[26]J. Lind, F. Fetzer, C. Hagenlocher, D. Blazquez-Sanchez, R. Weber, and T. Graf, "Transition from stable laser fusion cutting conditions to incomplete cutting analysed with high-speed x-ray imaging," J. Manuf. Processes **60**, 470–480 (2020).

[27]F. Reif, *Grundlagen der physikalischen Statistik und der Physik der Wärme* (de Gruyter, Berlin, 1976).